APPLIED SCIENCES AND ENGINEERING

Two-dimensional demixing within multilayered nanoemulsion films

Hye Min Seo[1]†, Seulwoo Kim[2]†, Sangwoo Kwon[2], YongJoo Kim[3], Minchul Sung[1], Jongryeol Yang[1], Boryeong Lee[1], Jongbaek Sung[2,4], Min-Ho Kang[5,6], Jungwon Park[2,4], Kyounghee Shin[1]*, Won Bo Lee[2]*, Jin Woong Kim[1]*

Benefiting from the demixing of substances in the two-phase region, a smart polymer laminate film system that exhibits direction-controlled phase separation behavior was developed in this study. Here, nanoemulsion films (NEFs) in which liquid nanodrops were uniformly confined in a polymer laminate film through the layer-by-layer deposition of oppositely charged emulsion nanodrops and polyelectrolytes were fabricated. Upon reaching a critical temperature, the NEFs exhibited a micropore-guided demixing phenomenon. A simulation study based on coarse-grained molecular dynamics revealed that the perpendicular diffusion of oil droplets through the micropores generated in the polyelectrolyte layer is crucial for determining the coarsening kinetics and phase separation level, which is consistent with the experimental results. Considering the substantial advantages of this unique and tunable two-dimensional demixing behavior, the viability of using the as-proposed NEF system for providing an efficient route for the development of smart drug delivery patches was demonstrated.

INTRODUCTION

Thermodynamic demixing leads to the formation of phase-separated microscopic domains either via discrete nucleation or spinodal decomposition (1–4). In addition, the demixing of soft materials can kinetically arrest metastable states or morphologies during phase separation (5–7). This simple principle has been widely applied to fine-tune polymer architectures (8–11), harden metal alloys (12, 13), and store energy in carbon materials (14–16). Notably, unlike three-dimensional bulk metaphase materials, the demixing of two-dimensional thin films is typically guided by surface-directed spinodal decomposition in which the material substrate in contact with the film substrate preferentially interacts with one of the components of the binary phase (17). In this process, the interplay between wetting and decomposition affects the dissipative dynamics, thereby determining the film microstructures and consequent functionalities (18–20).

In principle, the liquid-liquid demixing of a thin film occurs via a spontaneous, spinodal process, yielding a bicontinuous phase within the spinodal line, or proceeds via an activated nucleation and growth within the binodal and spinodal lines. The microstructure of a single-layer film can be theoretically predicted by considering the quenching depth, film dimension, and diffusivity of the nonwetting phase (21–23). Stacking the single layers enables the fabrication of a laminated structure; this is a highly desirable structural integration because the barrier performance for a given application solely depends on the number of layers, which determines the diffusivity (24–26). In addition to this laminate film structure, the phase transition dynamics, typically tuned using the demixing phenomenon,

are critical for manipulating the release kinetics of encapsulates or adsorbents through interlayer diffusion. Therefore, methods to fabricate laminate thin films that exhibit microphase separation in response to external stimuli for the intelligent release of active ingredients are required to develop widely applicable, high-performance delivery systems.

RESULTS

Fabrication of NEFs using layer-by-layer deposition

In this study, a previously unidentified type of two-dimensional demixing behavior in liquid nanodrop–confined multilayered polymer laminate films was demonstrated. For use as a model multilayered binary film with a metastable phase, a nanoemulsion film (NEF) was fabricated using the layer-by-layer (LbL) deposition of oppositely charged emulsion nanodrops and polyelectrolytes (Fig. 1A). First, an extremely stable oil-in-water (O/W) nanoemulsion was prepared. The nanoemulsion had an amphiphilic block copolymer (ABC), poly(ethylene oxide)-*block*-poly(ε-caprolactone) (PEO-*b*-PCL), and was coassembled with lecithin (Lipoid P75-3) to form a negatively charged resilient membrane at the interface. Using this preparation method, two sets of nanoemulsions with average hydrodynamic drop sizes of approximately 150 and 200 nm were obtained (Fig. 1, B to D). An alternative LbL deposition was conducted with the nanoemulsion drops and a polyelectrolyte [poly(diallyldimethylammonium chloride) (PDADMAC)] (Fig. 1E). The mass fraction of the oil in the NEF, NEF_ϕ, was determined using the internal standard method (fig. S1) (27). The NEF_ϕ could be adjusted by depositing nanoemulsions of different mean drop sizes: $NEF_{0.34}$ and $NEF_{0.82}$ were obtained using the 150- and 200-nm nanoemulsions, respectively. The NEF displayed a bumpy surface morphology according to the length scale of the oil droplet but appeared smooth at the micrometer scale (Fig. 1F). After a scratch was made on the NEF, it was observed using atomic force microscopy (AFM). The results showed that the film thickness increased linearly with the number of emulsion layers, which supports the inference that NEF was successfully produced through LbL deposition (Fig. 1G and fig. S2).

[1]School of Chemical Engineering, Sungkyunkwan University, Suwon 16419, Republic of Korea. [2]School of Chemical and Biological Engineering and Institute of Chemical Process, Seoul National University, Seoul 08826, Republic of Korea. [3]School of Advanced Materials Engineering, Kookmin University, Seoul 02707, Republic of Korea. [4]Center for Nanoparticle Research, Institute for Basic Science (IBS), Seoul 08826, Republic of Korea. [5]Department of Biomedical-Chemical Engineering, Catholic University of Korea, Bucheon 14662, Republic of Korea. [6]Department of Biotechnology, Catholic University of Korea, Bucheon 14662, Republic of Korea.
*Corresponding author. Email: sca680@skku.edu (K.S.); wblee@snu.ac.kr (W.B.L.); jinwoongkim@skku.edu (J.W.K.)
†These authors contributed equally to this work.
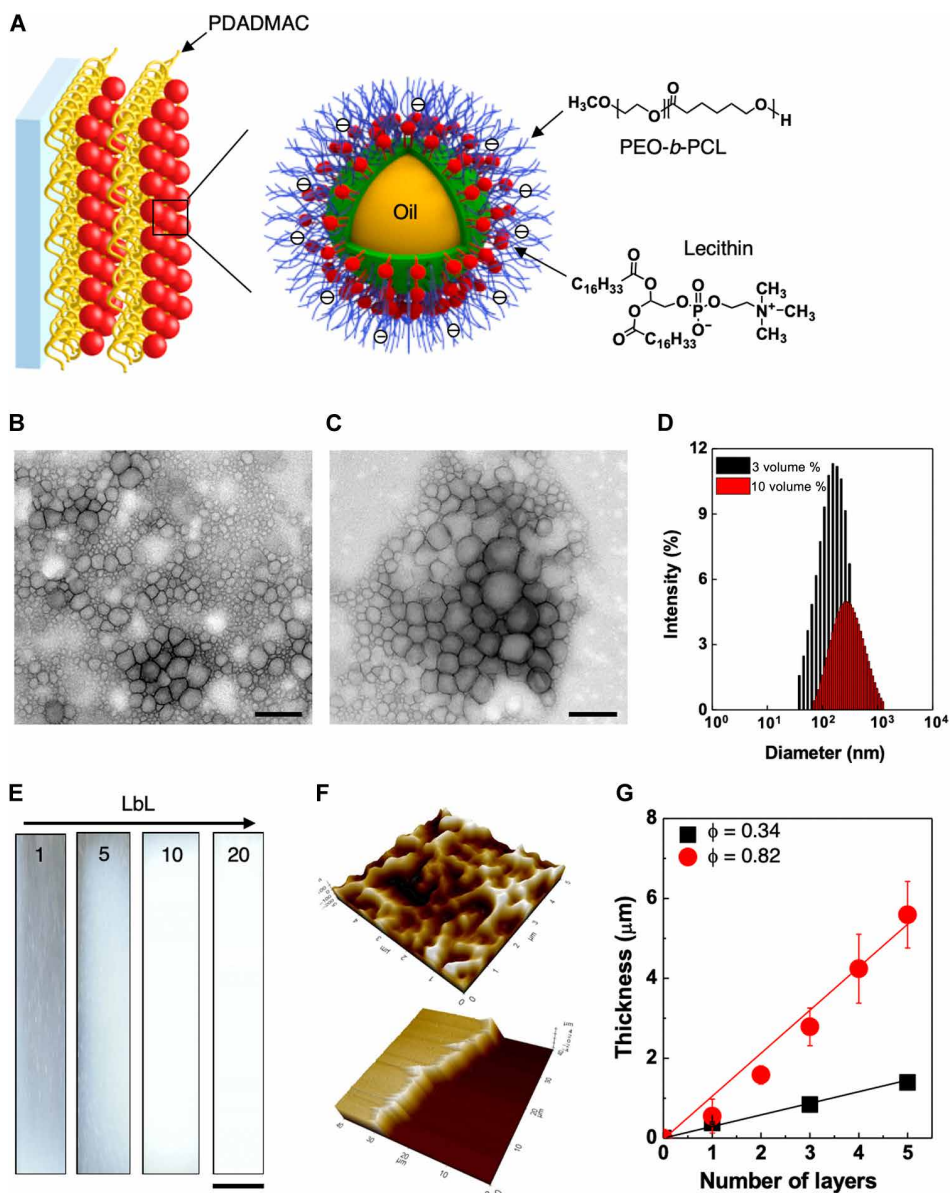
Fig. 1. Fabrication of NEFs using LbL deposition. (**A**) Schematic of the fabrication of an NEF using the LbL deposition of nanoemulsion drops and polyelectrolyte (PDADMAC) on a plasma-treated polyethylene terephthalate film. (**B** to **D**) Transmission electron microscopy images and size distributions of the 150- and 200-nm emulsion drops. Scale bars, 200 nm. (**E**) Appearance of $NEF_{0.34}$ with increasing number of emulsion layers. Scale bar, 1 cm. (**F**) AFM images of an unscratched $NEF_{0.34}$ (top) and a scratched $NEF_{0.34}$ (bottom). $NEF_{0.34}$-L5 was used for these observations. (**G**) Changes in film thickness with increasing number of layers.

Effect of annealing temperature on the demixing of NEFs

Notably, the as-fabricated NEFs exhibited demixing-based phase transformation behavior. To precisely determine the changes in the demixing behavior in response to the heat applied to the NEF, the phase images of the NEFs after thermal annealing at given temperatures were observed (Fig. 2 and fig. S3). The homogenous phase transformed into a heterogeneous phase while forming a bicontinuous structure at a critical annealing temperature, T_c, which depends on NEF_ϕ. Above T_c, the NEFs formed a droplet-type morphology at the micrometer scale. After reaching an equilibrium, the final oil domain size increased with increasing annealing temperature. The z-stack observations of confocal laser scanning microscope for single-layered NEFs above T_c showed that the oil domains grew by integrating

nanodrops around the primitive nucleus drops through coarsening. However, because demixing occurs in the polyelectrolyte-sandwiched layer, the growth of the oil domain is constrained by spatial limitations. Adequate evidence has been found in the case of $NEF_{0.82}$, wherein because the oil nanodrops are more concentrated, the oil domains grow to sizes larger than the interlayer thickness, thereby experiencing deformation from spherical globules to disk-shaped drops (fig. S4).

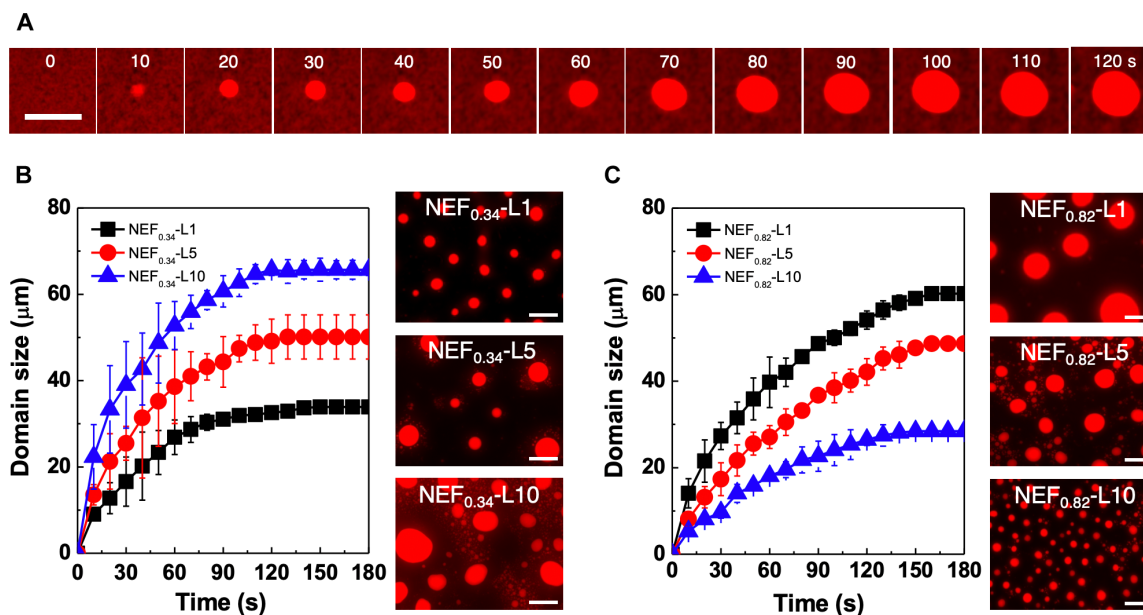## Phase separation kinetics of NEFs

According to the Cahn-Hilliard equation, the phase separation kinetics of a binary system is determined by the thermal diffusivity of the coarsening phase (*28*). Therefore, the coarsening behavior of

NEFs attributed to the amplitude of the concentration fluctuation with time (7) was investigated via the time-lapse monitoring of the oil domain generation and growth over the evolution time above $T_c = 80°C$. Although it is difficult to directly prove that the oil domain generation in the early stage remains unchanged with time for the NEF considered in this study, beyond the early stage, the coarsening of the oil domains has been observed. The domain size, $l(t)$, grows with time following a power law: as $l(t) \approx d_0 t^\alpha$, where d_0 is the prefactor related to the local viscosity, interfacial tension, and geometric constraints. In a solid binary mixture system, droplet coagulation yields $l(t) \approx d_0 t^{1/2}$ for a two-dimensional solid film system and $l(t) \approx$ $d_0 t^{1/3}$ for a three-dimensional solid system (29). In contrast, for a fluid system, $l(t) \approx d_0 t^{1/3}$, which is valid for any domain growth occurring in association with diffusion (30). The oil domain size of NEFs grew with scaling from $t^{0.43 - 0.57}$ (fig. S5). This range of power indices is higher than that of a three-dimensional solid system or a fluid system but close to that of a two-dimensional solid system, which is because NEF is a polyelectrolyte thin film system. The oil domain growth, which slightly exceeded $t^{0.5}$, is due to the presence of the NEF surface. After a sufficient growth stage was attained, the growth of the oil domain sizes plateaued (Fig. 3A and movies S1 and S2). Enhancing the thermal diffusion resulted in larger oil domains,
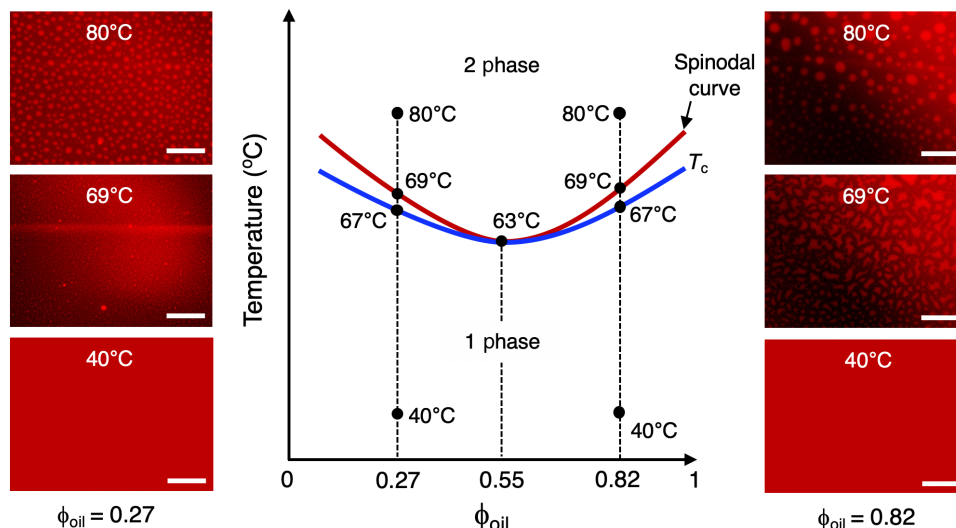

Fig. 2. Annealing temperature–dependent demixing of NEFs. Schematic phase diagram of the NEF-L1 samples. Fluorescence microscopy images of NEFs were taken after full decomposition at different annealing temperatures. Scale bars, 200 μm. For these observations, a fluorescence probe (Nile red) was encapsulated in the NEFs [0.001 weight % (wt %) in oil].

Fig. 3. Phase separation kinetics of NEFs. (**A**) Time-lapse fluorescence images of the coarsening oil domain of NEF$_{0.34}$-L5 at 80°C. Scale bar, 50 μm. Phase separation kinetics of NEFs depending on the number of layers: (**B**) NEF$_{0.34}$ and (**C**) NEF$_{0.82}$. Fluorescence images were obtained after full decomposition. Scale bars, 50 μm. In the NEF$_\phi$-Lα, ϕ is the oil mass fraction in the NEF, and α is the number of layers.

which is an irreversible process (fig. S6). Conventional demixing films thicker than 100 nm indicate diffusive bulk pattern growth in which the slope pattern is pinned at domain size scales of tens of micrometers owing to surface tension–driven viscous flow coarsening

(31, 32). With thicknesses ranging from hundreds of nanometers to several micrometers, the developed NEFs also exhibited similar pinning, thereby enabling the control of the long-lived metastable film state. In contrast to the conventional demixing exhibited by
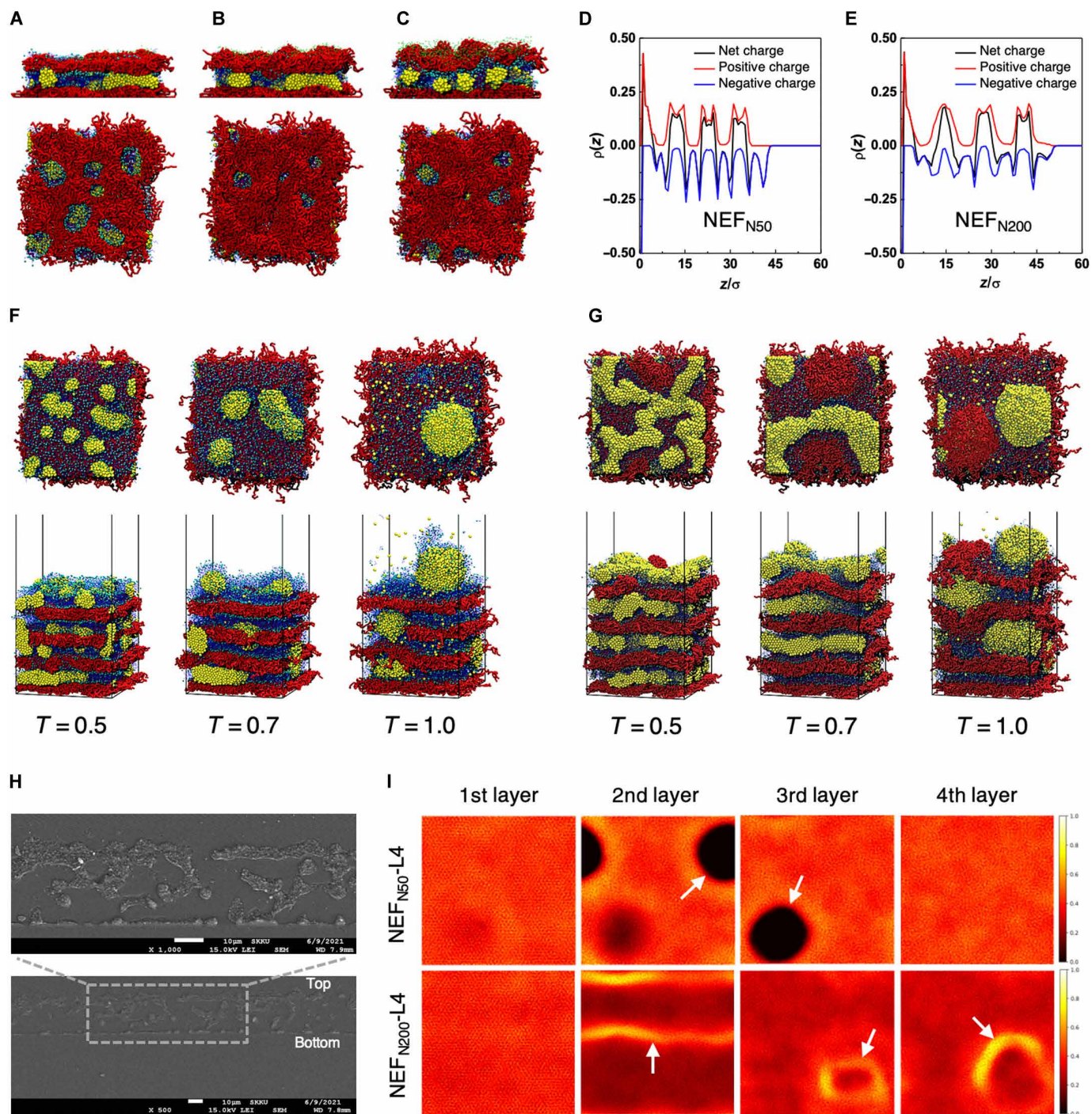
Fig. 4. Molecular dynamics modeling of NEFs. (**A** to **C**) Schematic of the deposition of charged chains. Note that the counter ions in the island phase are clumped together with the chains compared to the other phases. (A) Unsaturated film. (B) Saturated film. (C) Undulated surface film. (**D** and **E**) Local charge density along the z direction of NEF$_{N50}$ and NEF$_{N200}$. (**F** and **G**) Equilibrated NEFs for each temperature obtained using molecular dynamics simulations (red, positively charged chains; blue, ABC chains; yellow, oil particles; cyan, negatively charged particles at the end of ABC chains; green, negatively charged counter ions; positively charged counter ions are not shown in this figure.) (**H**) Scanning electron microscopy images of ultramicrotomed NEF$_{0.34}$-L20 embedded in a resin. (**I**) Density maps of positive charges in the polyelectrolyte in each layer of NEF$_{N50}$ and NEF$_{N200}$ at $T = 1.0$ ε/k_b. Dark phase corresponds to the micropores.

other composite films, the NEFs displayed unique phase-separation kinetics that were dependent on the number of layers. For a low NEF_ϕ (i.e., 0.34), the phase separation rate increased with increasing number of layers, and eventually, large oil domains were generated. However, for a high NEF_ϕ, such as 0.82, the phase separation rate and final oil domain size are inversely related to the number of layers (Fig. 3, B and C). For the intermediate NEF_ϕ of ~0.5, no significant dependence on the number of layers was observed (fig. S7).
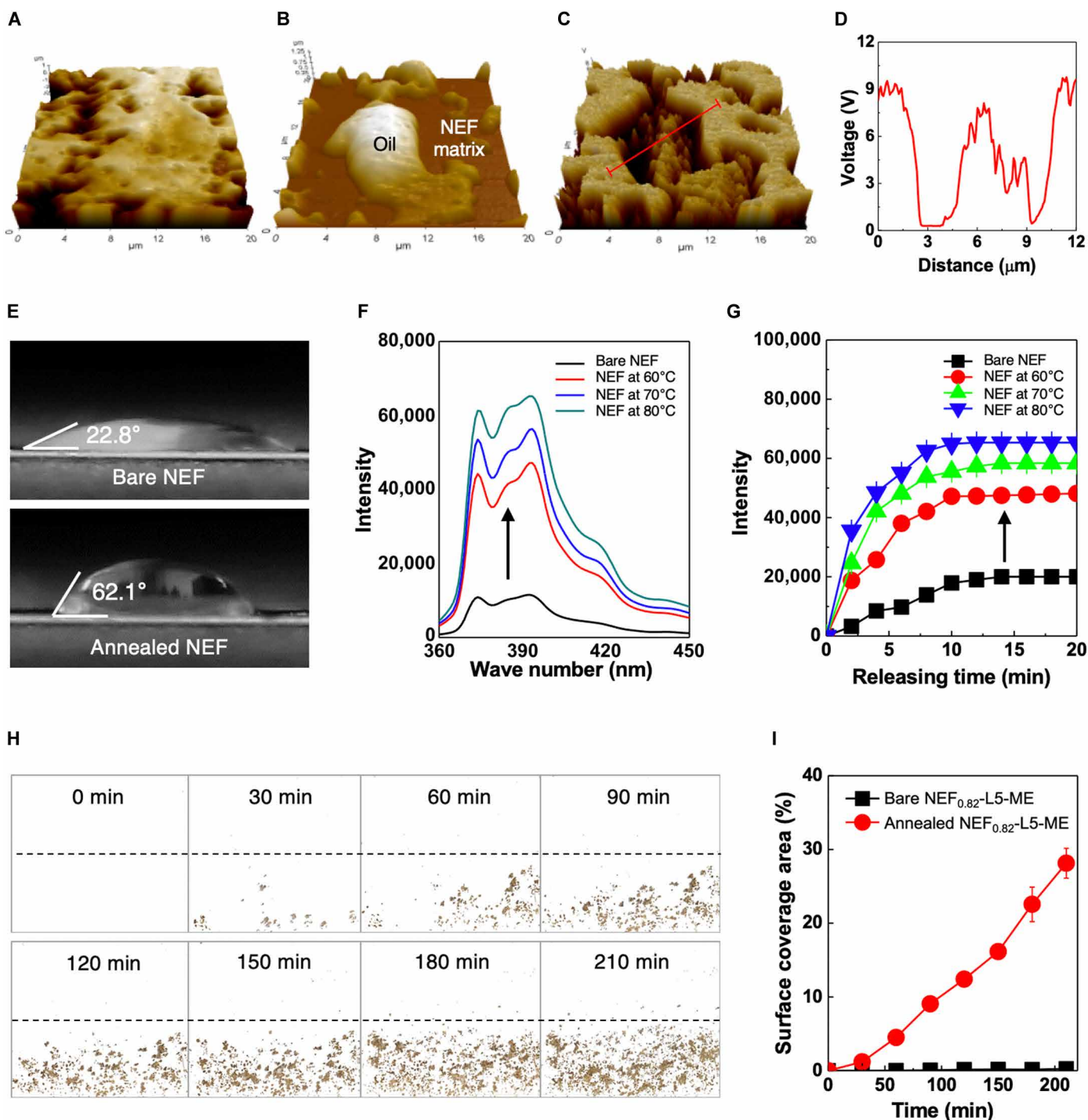
Fig. 5. Smart drug delivery performance of NEFs. (**A** and **B**) AFM surface topology before and after phase separation and (**C** and **D**) the EFM surface potential image and corresponding line profile. (**E**) Contact angles before (top) and after (bottom) phase separation. (**F**) Ultraviolet absorbance spectra of a model drug (pyrene) released at different annealing temperatures. (**G**) Temperature-responsive pyrene release. (**H**) Surface coverage of sand grains on ME-loaded $NEF_{0.82}$-L5 by ants: bare $NEF_{0.82}$-L5-ME (top) and $NEF_{0.82}$-L5-ME annealed at 80°C (bottom). NEF was produced using a nanoemulsion containing 0.03 wt % of ME, and the number of ants was 32. (**I**) Change in surface coverage with time.

This phase separation kinetics was also observed on curved substrates regardless of the curvature (figs. S8 and S9). These unexpected results imply that NEF_ϕ and the number of layers critically affect the coarsening process in a completely different manner.

Molecular dynamics modeling of NEFs

Coarse-grained molecular dynamics simulations were conducted to thoroughly understand the anomalous phase separation behavior of the NEFs (33, 34). To present a coherent explanation with the experimental results, the droplet sizes for the simulations of the nanoemulsions were varied while maintaining the other conditions constant. The low and high NEF_ϕ values correspond to NEF_{N50} consisting of 50 oil particles and NEF_{N200} consisting of 200 oil particles, respectively. In the process of developing the NEF system through LbL deposition modeling, it was found that the deposition of sufficient amounts of polyelectrolyte chains is required to produce a surface tension that can effectively retain the local charge neutrality against the predeposited base layer of the countercharged nanoemulsion drops (Fig. 4, A to C). The calculation of the charge density profiles of the NEFs perpendicular to the films (z direction) allowed us to postulate that the distance between the NEF layers was very small such that it could possibly result in electrostatic disturbances that would generate structural dislocations (Fig. 4, D and E).

This modeling study showed that micropores, which are large pores with sizes in the micrometer scale, are present throughout the NEF layers and that they assimilate the oil domains (Fig. 4, G and F; figs. S10 to S13; and movies S1 to S6). In the actual experiment, the formation of micropores was confirmed using the scanning electron microscopy imaging of the ultramicrotomed NEF embedded in a resin (Fig. 4H and fig. S14). The micropores of NEF_{N50} remained unchanged when the temperature was increased from $T = 0.5$ to $1.0\ \varepsilon/k_b$. As can be observed in the net charge density profiles, NEF_{N50} had a higher charge density than NEF_{N200} near the interface. Therefore, the higher energy barrier provided by the electrostatic potential prevented the positively charged layer from recovering open micropores, even at high temperatures. Notably, in our simulation, the micropores present in NEF_{N200} disappeared at $T = 1.0\ \varepsilon/k_b$. Moreover, the two-dimensional density map of each polyelectrolyte layer shows that the micropores generated in each NEF layer were filled with polyelectrolytes at high temperatures ($T = 1.0\ \varepsilon/k_b$), mainly because of the lower energy barrier of NEF_{N200} (Fig. 4I and figs. S15 to S18). The presence of micropores affected the diffusion behavior of the oil domains. These microstructural changes in NEFs during demixing determined the dimensions of the oil domain; i.e., when interlayer diffusion was dominant, an increase in the number of NEF layers led to the formation of larger oil domains, whereas when intralayer diffusion was dominant, the formation of oil domains followed the opposite pattern.

Smart drug delivery performance of NEFs

Demixing causes a notable change in the surface structure of NEFs, altering their physicochemical properties. Considering this fact, the most substantial observation was that the exposure of oil domains fractionated the NEF surface into hydrophilic and hydrophobic regions and, consequently, changed the surface wettability, which was verified using AFM (Fig. 5, A and B), electrostatic force microscopy (EFM) (Fig. 5, C and D), and Cassie-Baxter contact angle measurements (Fig. 5E) (35). This unique temperature-responsive phase separation behavior can facilitate the application of NEFs in smart drug release. To verify this point, NEF was prepared using a nanoemulsion containing pyrene as a proxy for the drug, and its temperature-responsive release was monitored (Fig. 5, F and G). As the annealing temperature approached T_c, the amount of pyrene released by NEF increased. With a further increase in the annealing temperature, the amount released also increased, thereby conforming to the phase separation pattern. This finding suggests a methodology comprising an intelligent technique for the release of drugs from thin-film drug cargos. To demonstrate this application, a multilayered NEF was fabricated on a glass slide using a nanoemulsion containing the insect-repellent methyl eugenol (ME; $NEF_{0.82}$-L5-ME; fig. S19). After placing it in an ant trap filled with sand grains, the reaction of the ants to the release of ME from $NEF_{0.82}$-L5-ME was monitored (movies S7 and S8). The ants in the trap with the bare $NEF_{0.82}$-L5-ME–coated slide did not exhibit any unusual behavior. In contrast, the ants in the trap with the annealed $NEF_{0.82}$-L5-ME–coated slide were covered with sand grains for 30 min. The ants continued to sand the slide surface for approximately 200 min and coated most of the surface before death (Fig. 5, H and I). This experiment demonstrated the practicability of using the NEF system in intelligent patch–type drug delivery applications.

DISCUSSION

Using a combination of experimental methodology and molecular dynamics simulations, this study identified and developed smart NEFs that exhibit intelligent temperature responses based on micropore-guided two-dimensional demixing. To the best of our knowledge, this is the first study that successfully demonstrates that a nanofluid-immobilized polymer thin film can exhibit unique phase separation behavior, which has notable technical utility. The unique phase-separation dynamics observed in the NEFs is attributed to the directional diffusion of oil nanodrops between or along their polyelectrolyte layers. Coarse-grain molecular dynamics simulations conducted to analyze the separation behavior revealed that the degree of interlayer interaction between stacks with opposite charges can generate micropores in the NEF, the formation or absence of which determines the demixing direction. This study also shows that NEFs are sensitive to the application of heat, which implies that engineering NEFs to function as a mode of delivery in administering life-saving drugs is a potential application of their smart release performance. The technique is expected to be applied to other thin-film systems, thereby enabling the design of new types of film composites through two-dimensional demixing–regulated topological physics or chemical reaction engineering.

MATERIALS AND METHODS
Materials

The PEO-b-PCL copolymer was supplied by ACT (PCL/PEO block = 1.07/1, $M_n \approx 10$ kDa, polydispersity index ≈ 1.37; South Korea). Lipoid P75-3 (phosphatidylcholine content, 70%; Lipoid Kosmetik AG, Germany) was used. Olive oil was purchased from Sigma-Aldrich (St. Louis, MO, USA). PDADMAC [$M_w = 2 \times 10^5$ to 3.5×10^5 g mol^{-1}, 20 weight % (wt %) in H$_2$O; Sigma-Aldrich, USA] was used as the cationic polyelectrolyte. Pyrene (98%) was used as a model drug, and Nile red (Sigma-Aldrich, USA) was used as a fluorescence probe. ME (Sigma-Aldrich, USA) was used as an insect repellent. The ants were sourced from Sciencetool (Seoul, South Korea). Deionized double-distilled water was used in all experiments.

Preparation of nanoemulsions

The nanoemulsion was prepared using the phase inversion composition method (36). First, to prepare the primary emulsion, PEO-*b*-PCL (0.5 g) and Lipoid P75-3 (0.1 g) were completely dissolved in tetrahydrofuran (7 ml) using sonication (Power Sonic 510, Hwashin, South Korea) for 10 min at 35°C. Subsequently, olive oil (1 ml) was added to this solution. During the vigorous stirring, phase inversion was induced by adding water (9 ml, 100 ml min⁻¹) to the mixture one drop at a time using a syringe pump (Pump 11 Elite, Harvard Apparatus, USA). The O/W emulsion generated after the phase inversion had a droplet size in the micrometer scale. After completely removing the tetrahydrofuran via evaporation at 40°C, the emulsion size was reduced to the nanoscale by applying strong sonication using a probe-type sonicator (20-kHz frequency, 130 W, VCX130, Sonic and Materials Inc., USA). The sonication duration was set to 5 min at 60% amplitude because no further size reduction was possible under these conditions.

Fabrication of NEFs via LbL deposition

First, a glass substrate (10 mm by 50 mm by 2 mm) was ultrasonicated in ethanol for 10 min, rinsed with water, and thoroughly dried. The glass slide was negatively charged through a plasma treatment (oxygen atmosphere, 0.1; 100 W for 10 min). The slide was then immersed in a PDADMAC aqueous solution (0.5 wt %) for 5 min and then fully rinsed with water to remove excess PDADMAC. Subsequently, the PDADMAC-coated substrate was immersed in the negatively charged nanoemulsion (3 or 10 wt % of olive oil, ζ potential ≈ −32 mV) for 5 min and then fully rinsed with water to produce a bilayer consisting of PDADMAC and emulsion drops on the glass slide. The LbL process was repeated to produce multilayered NEFs. NEF$_\phi$ was obtained using the internal standard method: NEF$_{0.34}$ and NEF$_{0.82}$ with 3 and 10 wt % of nanoemulsions, respectively (see the Supplementary Materials). The morphologies of the NEFs before and after phase separation were investigated using AFM operated in normal and electrical modes (EFM, XE-100, Park System, USA). The contact angles of water with the NEFs were measured using a charge-coupled device camera (Fainstec, STC-GEC83A, South Korea).

Monitoring the phase separation of NEFs

An NEF-coated glass slide was placed on a heating stage (freeze-heating stage, Agar Scientific, UK), and the phase separation behavior was observed using a fluorescence microscope (Axio Vert. A1, Carl Zeiss, Germany). To ensure immediate heat transfer, the heating stage was preheated to a designated temperature before mounting the NEF sample, and the observation was performed immediately after that. For each observation, a fluorescence image was obtained using a time-lapse software (1 snap/5 s).

Molecular dynamics simulation setup

Coarse-grained molecular dynamics simulations were conducted to study the phase behavior of the NEFs. The PDADMAC chain was modeled as 32 positively charged monomers, with a charge fraction of 0.2. The PEO-*b*-PCL ABC chain was modeled using four monomers, considering its relatively larger size compared to that of the PDADMAC chain. To simplify the system, we modeled lecithin (Lipoid P75-3) bound to PEO-*b*-PCL as a negatively charged single bead. All polymers were modeled on the basis of the simple bead spring model with a finite extensible nonlinear elastic bond potential between neighboring beads in a single chain, as presented in Eq. 1

(37). Other components, such as oil, surface, and counterions, were modeled as single beads

$$U_{\text{FENE}} = -0.5\, K R_0^2 \ln\left[1 - \left(\frac{r}{R_0}\right)^2\right], \text{where } K = 30\, \varepsilon\, \sigma^{-2} \text{ and } R_0 = 1.5\, \sigma \tag{1}$$

In this equation, ε and σ denote parameters for the bead spring model indicating the energy and length scale, respectively; r denotes the length of a bond; K denotes the strength of the bond; and R_0 denotes the maximum extent of the bond. The short-range nonbonding interaction is described using the 12-6 Lennard-Jones (LJ) potential and Coulombic potential, as presented in Eqs. 2 and 3, respectively

$$U_{\text{LJ}} = \begin{cases} 4\varepsilon\left[\left\{\left(\frac{\sigma}{r}\right)^{12} - \left(\frac{\sigma}{r}\right)^6\right\} - \left\{\left(\frac{\sigma}{r_c}\right)^{12} - \left(\frac{\sigma}{r_c}\right)^6\right\}\right], r \leq r_c \\ 0, r > r_c \end{cases} \tag{2}$$

$$U_{\text{coul}} = \frac{C q_i q_j}{r} \tag{3}$$

Two types of cutoff distances (r_c) for the LJ potential were selected: $r_c = 2.5\sigma$ for the standard LJ potential and $r_c = \sqrt[6]{2}\,\sigma$ for the fully repulsive Weeks-Chandler-Anderson (WCA) potential (36). The values of the potential parameter ε of the LJ potential for all possible pairs of systems are listed in table S1. The cutoff distance for the electrostatic interaction was determined to be 10σ. Within the cutoff distance, the interaction was calculated using a simple Coulombic potential between the charges q_i and q_j. C is the energy-conversion constant. The particle-particle particle-mesh (PPPM) method was used for longer distances (37).

System development for molecular dynamics simulation

The molecular dynamics simulations were performed in constant pressure-temperature ensemble (NPT) to construct nanoemulsion droplets of different sizes. Each droplet consisted of 50 to 200 oil particles with a few ABC chains, as described above. These nanoemulsions were used in the subsequent simulations. The LbL deposition was modeled in a simulation box with dimensions of 40σ by 40σ by 150σ and periodic boundary conditions in the x and y directions. Along the z direction, an imaginary slab with a length of $L = 3L_z$ was applied to accurately calculate the long-range electrostatic interaction using the PPPM solver. The top and bottom surfaces were composed of closely packed immobile particles, where the particles at the bottom surface were negatively charged with a charge density of 0.5. Positively charged PDADMAC chains were deposited onto the negatively charged bottom surfaces. In this step, an appropriate amount of PDADMAC chains was inserted to minimize fluctuations in the polyelectrolyte layer. Next, hexagonally aligned presimulated nanoemulsions and additional ABCs were added. ABCs were added to balance the local charge neutrality at the periphery of the emulsion drop. Using the two-step deposition process, a single bilayer was produced at a temperature of 0.5ε/k_b. During each single-layer deposition process, the same quantity of counter ions was added to ensure charge neutrality. A constant force of −0.5ε/σ along the z direction was applied to all particles during the layer deposition process, thereby stabilizing the thin film. Each step of the layer deposition process was conducted for 5000 τ and

integrated over time with $\Delta t = 0.006\ \tau$ using the velocity-Verlet algorithm. The temperature was maintained using a Langevin thermostat. The number of molecules in each deposition layer is listed in tables S2 and S3. This deposition process was repeated four times to form a multilayer NEF. Each NEF system was equilibrated at $T = 0.5\ \varepsilon/k_b$ for 50,000 τ under the conditions where the additional force was removed along the z direction, and the time step was set to 0.012 τ. The equilibrated configurations were then heated at $T = 0.7$ and 1.0 ε/k_b for 50,000 τ. All simulations were conducted using the LAMMPS open-source software with graphics processing unit (GPU) acceleration (40).

Experimental demonstration of smart drug release

To fabricate the insect repellent-NEFs, an LbL deposition was performed using a nanoemulsion containing 0.3 wt % of ME on a glass slide (76 mm by 26 mm by 1 mm). In this study, $NEF_{0.82}$ was used. Subsequently, two sets of NEF samples, bare $NEF_{0.82}$-L5-ME and $NEF_{0.82}$-L5-ME, annealed at 80°C for 10 min, were prepared. The NEFs were placed in a transparent plastic cubic box (20 cm by 20 cm by 20 cm) in which 32 ants were trapped at room temperature. The degree to which the ants covered the surface of the NEF-coated glass slide with sand grains was observed over time and characterized using an image analysis tool (Adobe Photoshop CS6).

SUPPLEMENTARY MATERIALS

REFERENCES AND NOTES

1. J. W. Cahn, On spinodal decomposition. *Acta Mater.* **9**, 795–801 (1961).
2. J. W. Schmelzer, A. S. Abyzov, J. Moller, Nucleation versus spinodal decomposition in phase formation processes in multicomponent solutions. *J. Chem. Phys.* **121**, 6900–6917 (2004).
3. R. Shimizu, H. Tanaka, A novel coarsening mechanism of droplets in immiscible fluid mixtures. *Nat. Commun.* **6**, 7407 (2015).
4. M. E. Hubert I. Aaronson, Jong K. Lee, *Mechanisms of Diffusional Phase Transformations in Metals and Alloys* (CRC Press, ed. 1, 2010).
5. J. Fan, T. Han, M. Haataja, Hydrodynamic effects on spinodal decomposition kinetics in planar lipid bilayer membranes. *J. Chem. Phys.* **133**, 235101 (2010).
6. L. Li, X. Shen, S. W. Hong, R. C. Hayward, T. P. Russell, Fabrication of co-continuous nanostructured and porous polymer membranes: Spinodal decomposition of homopolymer and random copolymer blends. *Angew. Chem. Int. Ed. Engl.* **51**, 4089–4094 (2012).
7. J. T. Cabral, J. S. Higgins, Spinodal nanostructures in polymer blends: On the validity of the Cahn-Hilliard length scale prediction. *Prog. Polym. Sci.* **81**, 1–21 (2018).
8. S. Yoo, J. H. Kim, M. Shin, H. Park, J. H. Kim, S. Y. Lee, S. Park, Hierarchical multiscale hyperporous block copolymer membranes via tunable dual-phase separation. *Sci. Adv.* **1**, e1500101 (2015).
9. L. Ruiz-Pérez, L. Messager, J. Gaitzsch, A. Joseph, L. Sutto, F. L. Gervasio, G. Battaglia, Molecular engineering of polymersome surface topology. *Sci. Adv.* **2**, e1500948 (2016).
10. T. Kietzke, D. Neher, K. Landfester, R. Montenegro, R. Guntner, U. Scherf, Novel approaches to polymer blends based on polymer nanoparticles. *Nat. Mater.* **2**, 408–412 (2003).
11. K. V. Peinemann, V. Abetz, P. F. Simon, Asymmetric superstructure formed in a block copolymer via phase separation. *Nat. Mater.* **6**, 992–996 (2007).
12. Z. Chen, X. Wang, Y. Qi, S. Yang, J. A. Soares, B. A. Apgar, R. Gao, R. Xu, Y. Lee, X. Zhang, J. Yao, L. W. Martin, Self-assembled, nanostructured, tunable metamaterials via spinodal decomposition. *ACS Nano* **10**, 10237–10244 (2016).
13. A. K. da Silva, D. Ponge, Z. Peng, G. Inden, Y. Lu, A. Breen, B. Gault, D. Raabe, Phase nucleation through confined spinodal fluctuations at crystal defects evidenced in Fe-Mn alloys. *Nat. Commun.* **9**, 1137 (2018).
14. C. Jo, J. Hwang, W. G. Lim, J. Lim, K. Hur, J. Lee, Multiscale phase separations for hierarchically ordered macro/mesostructured metal oxides. *Adv. Mater.* **30**, 1703829 (2018).
15. T. Liu, Z. Zhou, Y. Guo, D. Guo, G. Liu, Block copolymer derived uniform mesopores enable ultrafast electron and ion transport at high mass loadings. *Nat. Commun.* **10**, 675 (2019).
16. P. Adelhelm, Y. S. Hu, L. Chuenchom, M. Antonietti, B. M. Smarsly, J. Maier, Generation of hierarchical meso- and macroporous carbon from mesophase pitch by spinodal decomposition using polymer templates. *Adv. Mater.* **19**, 4012–4017 (2007).
17. M. B. Wise, P. C. Millett, Two-dimensional bicontinuous structures from symmetric surface-directed spinodal decomposition in thin films. *Phys. Rev. E* **98**, 022601 (2018).
18. R. Kurita, Control of pattern formation during phase separation initiated by a propagated trigger. *Sci. Rep.* **7**, 6912 (2017).
19. Y. Matsuura, F. Yoshii, T. Otsuka, K. Kadowaki, M. Ijiri, Y. Takemoto, K. Terashima, T. Wakita, T. Yokoya, Y. Muraoka, Multilayer formation via spinodal decomposition in TiO_2-VO_2 epitaxial films on sapphire substrates. *J. Eur. Ceram. Soc.* **38**, 5043–5050 (2018).
20. P. Das, P. K. Jaiswal, S. Puri, Surface-directed spinodal decomposition on chemically patterned substrates. *Phys. Rev. E* **102**, 012803 (2020).
21. H. Wang, R. J. Composto, Thin film polymer blends undergoing phase separation and wetting: Identification of early, intermediate, and late stages. *J. Chem. Phys.* **113**, 10386–10397 (2000).
22. E. P. Feldman, L. I. Stefanovich, Y. V. Terekhova, Influence of adsorption or desorption and surface diffusion on the formation kinetics of open half-monolayer coverage. *Phys. Rev. E* **89**, 062406 (2014).
23. A. Goyal, P. van der Schoot, F. Toschi, Impact of the prequench state of binary fluid mixtures on surface-directed spinodal decomposition. *Phys. Rev. E* **103**, 042801 (2021).
24. L. A. Yang, T. C. Suo, Y. H. Niu, Z. G. Wang, D. Yan, H. Wang, Effects of phase behavior on mutual diffusion at polymer layers interface. *Polymer* **51**, 5276–5281 (2010).
25. I. Povstugar, P. P. Choi, D. Tytko, J. P. Ahn, D. Raabe, Interface-directed spinodal decomposition in TiAlN/CrN multilayer hard coatings studied by atom probe tomography. *Acta Mater.* **61**, 7534–7542 (2013).
26. J. Park, G.-Y. Kim, K. Song, S.-Y. Choi, J. Son, Self-assembly of correlated (Ti, V)O_2 superlattices with tunable lamella periods by kinetically enhanced spinodal decomposition. *NPG Asia Mater.* **11**, 32 (2019).
27. D. Pigini, A. M. Cialdella, P. Faranda, G. Tranfo, Comparison between external and internal standard calibration in the validation of an analytical method for 1-hydroxypyrene in human urine by high-performance liquid chromatography/tandem mass spectrometry. *Rapid Commun. Mass Spectrom.* **20**, 1013–1018 (2006).
28. J. W. Cahn, J. E. Hilliard, Free energy of a nonuniform system. I. Interfacial free energy. *J. Chem. Phys.* **28**, 258–267 (1958).
29. S. K. Das, S. Puri, J. Horbach, K. Binder, Molecular dynamics study of phase separation kinetics in thin films. *Phys. Rev. Lett.* **96**, 016107 (2006).
30. S. K. Das, S. Roy, J. Midya, Coarsening in fluid phase transitions. *C. R. Phys.* **16**, 303–315 (2015).
31. I. M. Lifshitz, V. V. Slyozov, The kinetics of precipitation from supersaturated solid solutions. *J. Phys. Chem. Solid* **19**, 35–50 (1961).
32. L. Sung, A. Karim, J. F. Douglas, C. C. Han, Dimensional crossover in the phase separation kinetics of thin polymer blend films. *Phys. Rev. Lett.* **76**, 4368–4371 (1996).
33. J. M. Carrillo, A. V. Dobrynin, Layer-by-layer assembly of polyelectrolyte chains and nanoparticles on nanoporous substrates: Molecular dynamics simulations. *Langmuir* **28**, 1531–1538 (2012).
34. P. A. Patel, J. Jeon, P. T. Mather, A. V. Dobrynin, Molecular dynamics simulations of layer-by-layer assembly of polyelectrolytes at charged surfaces: Effects of chain degree of polymerization and fraction of charged monomers. *Langmuir* **21**, 6113–6122 (2005).
35. D. Murakami, H. Jinnai, A. Takahara, Wetting transition from the Cassie–Baxter state to the Wenzel State on textured polymer surfaces. *Langmuir* **30**, 2061–2067 (2014).
36. K. Shin, G. Gong, J. Cuadrado, S. Jeon, M. Seo, H. S. Choi, J. S. Hwang, Y. Lee, A. Fernandez-Nieves, J. W. Kim, Structurally stable attractive nanoscale emulsions with dipole-dipole interaction-driven interdrop percolation. *Chem. A Eur. J.* **23**, 4292–4297 (2017).
37. K. Kremer, G. S. Grest, Dynamics of entangled linear polymer melts: A molecular-dynamics simulation. *J. Chem. Phys.* **92**, 5057–5086 (1990).
38. D. C. John, D. Week, Role of repulsive force in determining the equilibrium structure of simple liquids. *J. Chem. Phys.* **54**, 5237–5247 (1970).
39. O. Buneman, Computer simulation using particles (R. W. Hockney and J. W. Eastwood). *SIAM Rev.* **25**, 425–426 (1983).
40. S. Plimpton, Fast parallel algorithms for short-range molecular dynamics. *J. Comput. Phys.* **117**, 1–19 (1995).